Hollow Plasma Acceleration Driven by a Relativistic Reflected Hollow Laser

W. P. Wang,[1,*,§] C. Jiang,[1,2,3,§] H. Dong,[1,3] X. M. Lu,[1] J. F. Li,[1] R. J. Xu,[1] Y. J. Sun,[1] L. H. Yu,[1] Z. Guo,[1] X. Y. Liang,[1] Y. X. Leng,[1] R. X. Li,[1,2,3,†] and Z. Z. Xu[1,‡]

[1]*State Key Laboratory of High Field Laser Physics and CAS Center for Excellence in Ultra-intense Laser Science, Shanghai Institute of Optics and Fine Mechanics (SIOM), Chinese Academy of Sciences (CAS), Shanghai 201800, China.*

[2]*School of Physical Science and Technology, ShanghaiTech University, Shanghai 201210, China*

[3]*University of Chinese Academy of Sciences, Beijing 100049, China*

(Received 18 October 2019; revised 21 June 2020; accepted 30 June 2020; published 17 July 2020)

In order to address the present difficulty in experimentally generating the relativistic Laguerre-Gaussian laser, primarily due to damage caused to optical modulators, a high-reflectivity phase mirror is applied in the femtosecond petawatt laser system to generate a relativistic hollow laser at the highest intensity of 6.3×10^{19} W/cm^2 for the first time. A simple optical model is used to verify that the vortex laser may be generated in this new scheme; using such a relativistic vortex laser, the hollow plasma drill and acceleration are achieved experimentally and proven by particle-in-cell simulations. With the development of the petawatt laser, this scheme opens up possibilities for the convenient production of the relativistic hollow laser at high repetition and possible hollow plasma acceleration, which is important for a wide range of applications such as the generation of radiation sources with orbital angular momentum, fast ignition for inertial confinement fusion, and jet research in the astrophysical environment.

DOI: 10.1103/PhysRevLett.125.034801

In 1992, Allen *et al.* recognized that vortex light with an azimuthal angle φ dependence of $\exp(-il\varphi)$, such as Laguerre-Gaussian (LG) light, carries orbital angular momentum (OAM) in the unit of $\hbar$ [1]; l is an integer value, positive or negative, and for any given l, the vortex light has l intertwined helical phase fronts, resulting in a phase singularity with zero intensity distribution on the beam axis. Thus, vortex light has a hollow-structure intensity distribution, which has been applied to manipulate micrometer-scale matter [2–4], as a special tweezer (2018 Nobel Prize in Physics) [5], and in microscopy and imaging [6,7], atomic and nanoparticle manipulation [8,9], optical communications [10,11], quantum computing [12], and astrophysics [13].

Nowadays, the laser intensity can significantly exceed 10^{18} W/cm^2 [14] with the development of chirped pulse amplification technology (2018 Nobel Prize in Physics) [15], which allows the previously weak LG light to be turned into a relativistic LG laser ($>10^{18}$ W/cm^2). Previously, transparent matter, such as latex, was usually trapped by the Fresnel deflection force when LG light irradiated on it [5]. However, for the high-intensity LG laser, the interacting mechanism changes entirely; the matter is ionized by the huge laser fields and manipulated by the hollow-structured pondermotive force. Thus, it is reasonable to consider that new particle manipulators can be achieved beyond classical tweezers, spanners, or wrenches, such as the relativistic vortex cutter [16] and hollow screwlike drill in plasma [17]. More recently, the relativistic vortex hollow laser has received significant attention in theorizing several concepts, such as donut wakefield acceleration [18–21], attosecond electron generation [22–26], proton acceleration [27,28], vortex harmonics generation [29,30], huge magnetic field generation [31–33], and Gamma ray generation [34,35].

However, it is difficult to experimentally generate the above-mentioned relativistic LG laser under present laboratory conditions, primarily owing to the damage caused to the optical modulators. Recently, researchers proposed plasma-based generation of a relativistic LG laser [36–39], which is not limited based on the intensity or power of the laser. However, this strictly depends on the formation of plasma with unique parameters for density and structure, which is very difficult to control in experiments, particularly those with high repetition rates. Therefore, there is a need to find reproducible and predictable approaches to generate a controllable high-repetition hollow LG laser in experiments to realize the novel physics conceptualized in the previous theoretical and simulated works.

In this study, the relativistic hollow vortex laser with the highest intensity of 6.3×10^{19} W/cm^2 is first generated by a reflected phase plate and then focused by a parabola in the experiments, which is verified by a simple transparent optical model. In the proof-of-principle experiment, it is found that the hollow-structure proton beam is generated and accelerated by such a hollow laser, which is significantly different from the case driven by the traditional Gaussian laser. Three-dimensional (3D) particle-in-cell (PIC) simulations are carried out to verify the experimental results, showing that the hollow structured proton beam is closely related to the hollow drill in plasma driven by the

vortex laser. Our research opens up the possibility of convenient production of a relativistic hollow laser with high repetition and possible hollow plasma acceleration, which can be used in a wide range of applications, as proven by the previous theoretical and simulated works.

In experiments, a traditional Gaussian laser [40–42] is incident on a reflected phase plate with 32 steps at an angle of 45° (with respect to the normal direction of the phase plate) which is then focused by a parabola mirror, generating a vortex hollow laser [see Fig. 1(a)]. The size of the high-reflectivity phase plate is 230×170 mm^2, the diameter of the incident laser is 150 mm, the laser energy is ~13 J, and the laser duration is ~40 fs. After the off-axis parabola (OAP), the radius of the focal spot and the hole at the laser axis is $r_f \sim 9$ and $r_h \sim 2$ μm [see Fig. 1(b)], respectively. The enclosed energy in the full width at half maximum (FWHM) of the focal spot is about 30%, and the laser intensity $I = \sim 6.3 \times 10^{19}$ W/cm^2 is obtained. For the LG laser mode (LG_p^l), l denotes the number of 2π phase cycles around the circumference, and $(p+1)$ denotes the number of radial nodes in the mode profile. In our case, to generate the $\mathrm{LG}_{p=0}^{l=1}$ mode laser, the depth of each step was designed to be $\Delta D = \lambda \sin 45°/32 \sim 17.5$ nm. The total depth from step 1 to 32 is $D = 32\Delta D \sim 556$ nm [see Fig. 1(d)]. Here, $\lambda \sim 790$ nm is the laser wavelength. From Fig. 1(b), it can be observed that a singularity point appears in the center of the laser intensity distribution at the focus, that is much different from the distribution of the Gaussian laser in Fig. 1(c). It shows that the laser distribution can be changed from Gaussian [see Fig. 1(c)] to hollow [Fig. 1(b)] by simply replacing the plane mirror with a phase plate in Fig. 1(a) in experiments. It should be noted that the spot of the Gaussian laser is not regular round enough [see Fig. 1(c)], indicating the beam quality is not perfect, which may cause the unclean distribution of the hollow shape for the LG laser [see Fig. 1(b)]. It is hoped to be cleaner if we further improve the beam quality of the incident Gaussian pulse in experiments in the future.

A transmitted optical model is used to verify that a hollow laser can be generated in this manner. The spatial profile of the incident laser is near flat-top with a diameter of 150 mm; the electric field of the circular polarized laser is $E(r,\theta) = E_r e^{i\theta}(\mathbf{e}_r \pm i\mathbf{e}_\theta)/\sqrt{2}$, where E_r is the axially symmetric amplitude distribution of beam and $\pm$ denotes the different circular polarization (CP). For simplicity, $E_r = 1$ is used in our model. The transmitted 32-step phase plate with expression of $e^{i\varphi}$ is used to mimic the action of the reflected phase plate in the experiments, where $\varphi = (m/32) \times 2\pi$, $[m\pi/16 < \theta < (m+1)\pi/16]$, $m = 0, 1, \ldots, 31$. A transmitted lens mimics the parabola mirror, where the focus length is 600 mm and the aperture diameter is 150 mm. Then, the field distribution of the laser beam near the focus can be obtained using the Huygens-Fresnel principle [43]:

$$E(P) = -\frac{i}{\lambda}\frac{Ae^{-ikf}}{f}\iint_W \frac{e^{iks}}{S}dS, \tag{1}$$

where P is a point near the laser focus, s is distance between points P and Q [Q is a point of the wave front (W) on the lens], and A/f is the amplitude of point P.

Figure 2 shows the calculation results according to Eq. (1), where $+$ is used; it is found that the laser is tightly focused near $z = 0$ μm. The diameter of the laser focal spot is ~120 μm at $z = -500$ μm [see Fig. 2(b)] and ~10 μm at $z = 0$ μm [see Fig. 2(c)], which is similar to the laser diameters in the experiments [see Fig. 1(b)]. The holes can be observed clearly in the beam axis in both theoretical calculations and experiments. Thus, it is proved that a hollow laser can be experimentally generated by a reflected phase plate and then focused by a parabolic mirror (see Fig. 1). In addition, Figs. 2(d) and 2(e) show the distributions of electric fields (Ex and Ey) at $z = 0$ μm, both of which have phases from $0 - 2\pi$ in the $x-y$ plane. This indicates that the $\mathrm{LG}_{p=0}^{l=1}$ mode laser may be generated and proves that the design of the reflected phase plate is practical in our case.

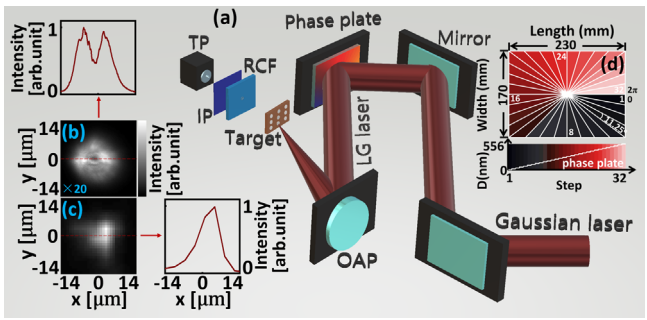

FIG. 1. (a) Experimental setup. Intensity distributions of the (b) LG and (c) Gaussian laser at focus. (d) Structure of the phase plate.

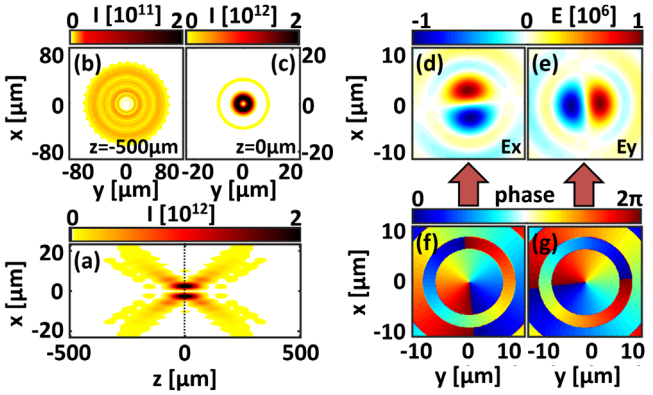

FIG. 2. Laser intensity distributions in (a) $x-z$ plane, $x-y$ planes at (b) $z = -500$ and (c) $z = 0$ μm. Distributions of electric field (d) Ex and (e) Ey at focus ($z = 0$ μm); (f) and (g) are the corresponding phase distributions of (d) and (e).

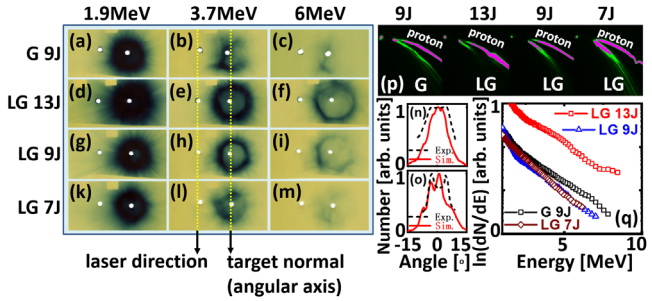

FIG. 3. Proton imaging on RCFs driven by (a)–(c) a Gaussian laser with 9 J, a LG laser with (d)–(f) 13, (g)–(i) 9, and (k)-(m) 7 J, respectively. Spatial distribution of protons on RCF in experiments (dash line) and simulations (solid line) for the case of (n) Fig. 3(d) and (o) Fig. 3(e). Here, the angular axis is the target normal direction determined by the laser focal spot and the hole on the RCF. (p) Images on the IP plate. (q) Energetic spectra in the case of a Gaussian laser with 9 J (black square), and a LG laser with 13 (red square), 9 (blue triangle), and 7 J (wine diamond) in experiments.

The proton accelerations driven by the LG (see Fig. 1) and Gaussian lasers are shown in Fig. 3. The image and spectra are recorded by radio chromic film (RCF) stacks and a Tomson spectrometer (TP), respectively [see Fig. 1(a)]. The distance between the target and RCF is $L_{\mathrm{T-RCF}} \sim 11$ cm, and the TP is ~53 cm away from the target. In these cases, the proton beams are mainly concentrated around the target normal direction [see Figs. 3(a)–3(m)], which is assumed to be accelerated by the shock acceleration mechanism [44,45]. The corresponding spectra of the proton beam can be obtained from the IP plate in Fig. 3(p). From Fig. 3(q), it can be observed that the maximum energy (~8.5 MeV) of the proton beam is obtained by the 13 J LG laser, which is close to the maximum energy driven by the *CP* Gaussian laser with similar laser intensity at the 10^{19} W/cm^2 level in our previous experiments [46]. The maximum energy decreases with the decreasing of the laser energy. About a 6 MeV proton beam is generated in the case of a 7 J LG laser (the corresponding laser intensity is 2×10^{19} W/cm^2). At the same time, it can be found that the fuzzier circle image of the proton beam is formed for the smaller energy of the LG laser. So, it indicates that we should use the LG laser with larger intensity to maintain the clear and complete circle shape in our experiments.

For the case of the Gaussian laser, maximum energy ~8 MeV is obtained in Fig. 3(q), where the laser energy is 9 J, the spot diameter of the laser focus is ~5 μm, and the laser intensity is $\sim 8.5 \times 10^{19}$ W/cm^2. Most of the protons are also concentrated around the target normal direction [see Figs. 3(a)–3(c)], which is similar to the cases of the LG laser [see Figs. 3(d)–3(m)]. However, the structure of the proton beam driven by the LG laser is significantly different from that of the Gaussian laser; a dot-structure proton beam is generated by the Gaussian laser, whereas in the case of the LG laser, a hollow proton beam is produced. All these results are repeatable in our experiments. It should be noted that the formation of the proton beam has a close relation with laser intensity, duration, polarization, and target material, thickness, and so on. In our case, we mainly research the 40-fs PW laser irradiating on the 80-nm thick foil, which is different from the ring-structured proton generations driven by the picosecond laser [47–49] in the previous experiments. In addition, the hollow plasma is generated when we only change the shape of the laser from Gaussian to hollow shape, which is also much different from the dot-structured beam driven by the Gaussian laser in our previous experiments [41,50–53]. So, it can be concluded that the hollow plasma may have a close relation to the hollow-structure distribution of laser intensity (see Fig. 1). Some novel physics may appear and require further research.

Then, 3D PIC simulations were carried out to illustrate the roles of the hollow vortex laser on the hollow proton acceleration. First, the 1D MULTI code was used to simulate the interaction between the laser prepulse and the 80-nm-thick plastic solid foil (initial density is 1.3 g/cm^3); see Fig. 4(a). Then the front part of the foil expands down to 0.09 g/cm^3 (~23 n_c) at $x \sim 4$ μm at the back side of the foil (the front side of the foil initially lies at $x = 0$ μm), see Fig. 4(b). Here $n_c = \omega^2 m_e / 4\pi e^2$ is the critical density, and the plastic layer is assumed to ionize to carbon ions, protons, and electrons. To be simple, the expanded plasma foil with ~1.8 μm thickness is used in PIC simulations, just as shown in Fig. 4(b). And the detail expression of the plasma density distribution can be fitted as $n_e(X) = (-21.6X^5 - 94.8X^4 - 143.1X^3 - 80.6X^2 - 0.3X + 15.3)n_c$, where $-1.5 < X < 0.3$, just as the inside plot in Fig. 4(b). $n_p(X) = 1/3n_e(X)$ and $n_C(X) = 1/6n_e(X)$ are used to described the density distribution of protons and C^{4+} ions, respectively. The size of the simulation box is 60 μm$(x) \times 60$ μm$(y) \times 60$ μm(z); the number of spatial grids is $600 \times 600 \times 600$, each of which is filled with 5 particles.

A 40-fs *CP* LG laser was incident from the left and irradiated the target at an angle of 15°. The fields of the *CP* LG laser can be simply expressed as

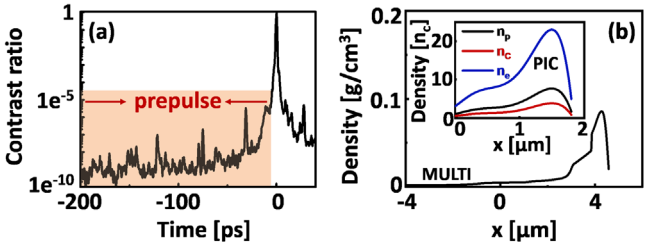

FIG. 4. (a) Profile of the laser in experiments. (b) Density distribution driven by the prepulse in a 1D MULTI simulation. The corresponding density of proton n_p (black), C^{4+} ions n_C (red), and electrons n_e (blue) is designed in the inset plot for the PIC simulations.

$$a_y(\mathrm{LG}_p^l) = a_0(-1)^p \exp\left[-\frac{r^2}{W_\perp^2}\right]\left(\frac{r\sqrt{2}}{W_\perp}\right)^l L_p^l \times \left(\frac{2r^2}{W_\perp^2}\right) g(x-ct)\cos[kx-\omega t+l\phi], \quad (2)$$

$$a_z(\mathrm{LG}_p^l) = a_0(-1)^p \exp\left[-\frac{r^2}{W_\perp^2}\right]\left(\frac{r\sqrt{2}}{W_\perp}\right)^l L_p^l \times \left(\frac{2r^2}{W_\perp^2}\right) g(x-ct)\cos\left[kx-\omega t+\frac{\pi}{2}+l\phi\right], \quad (3)$$

where $a_0 = eE_0/m_e\omega c = 3.9$ (corresponding to the laser intensity of $I \sim 6.3 \times 10^{19}$ W/cm^2) is the dimensionless peak amplitude of the laser pulse, e is the electron charge, E_0 is the peak amplitude of the electric field, m_e is the electron mass, and c is the speed of light in vacuum. The wavelength of the laser is $\lambda = 0.8$ μm, $W_\perp = 7$ μm is the radius at which the Gaussian term falls to $1/e$ times its on-axis value, L_p^l is the generalized Laguerre polynomial, $g(x-ct) = \cos^2[\pi(x-ct)/(2W_x)]$ for-$W_x < x - ct < W_x$, $W_x = 12$ μm is the pulse length in the x direction (corresponding to 40 fs), k is the wave number, ω is the laser frequency, x is distance from the beam waist, and ϕ is the azimuthal angle [54].

Figures 5(a)–5(i) show the interactive progress driven by the LG laser in detail. The LG laser arrives at the front surface of the target at $t \sim 45$ T, where T $= \lambda/c$ is the laser duration. The lower part ($y < 0$ μm) of the LG laser is first reflected by the obliquely placed target [see Fig. 5(a)], so the plasma there is preferentially accelerated [see Figs. 5(d) and 5(g)]. Then, the laser is totally reflected at $t = 80$ T [see Fig. 5(b)]. The protons simultaneously take on a hollow shape; however, the target back remains flat. The main

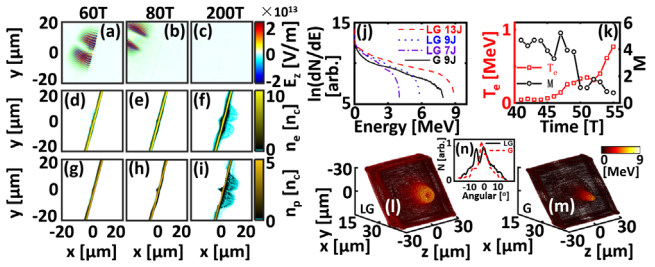

FIG. 5. Distributions of (a)–(c) electric field Ez, (d)–(f) electron density, (g)–(i) proton density at 60 (first row), 80 (second row), and 200 T (third row). (j) Proton spectra driven by a Gaussian laser with 9 J (solid line), a LG laser with 13 (dashed line), 9 (dotted line), and 7 J (dashed-dotted line) at $t = 200$ T. (k) Evolution of electron temperature (red square) and Mach number M (black circle). Energetic envelope of the proton layer driven by (l) a LG laser and (m) a Gaussian laser $t = 200$ T. (n) Angular distributions for LG (black solid line) and Gaussian laser (red dashed line).

reason for this is that the CP LG laser can reduce the electron heating to a certain extent during the hole-boring stage [55–58], such that less electrons are transported to the back, and the target normal sheath field acceleration [50,51,59] disappears on the back layer of the proton at that time. The plasma foil can be further accelerated up to the energy of ~9 MeV $t = 200$ T, which is similar to the experimental results in Fig. 3(q). It is assumed that the shock acceleration mechanism [45] plays a dominant role for the proton layer, because the Mach number $M = v_s/c_s > 1.5$ [see Fig. 5(k)] at the beginning of the interaction (41 T $< t <$ 50 T) satisfies the condition of electrostatic shocks [44].

Finally, the hollow-shaped proton beam can be obtained in the simulation shown in Figs. 5(i) and 5(l), which is significantly different from the case driven by the traditional Gaussian laser [see Fig. 5(m)]. The angular divergences of the proton beams are calculated in the 2D case [see Figs. 3(n), 3(o), and Fig. 5(n)] to compare the proton image on the RCFs in experiments. Here, the protons with energies from 1.9 to 2.9, 3.7 to 4.7, and 5 to 6 MeV are counted in the simulations to explain the cases of Figs. 3(d)–3(f), respectively. From Figs. 3(n) and 3(o), it can be found that the divergences of the proton beams are smaller than those obtained in the experiments. This may be affected by the fact that the laser or target qualities are not perfect in experiments as those in simulations. More important is that the angular distribution for lower energy (~1.9 MeV) around 0° (target normal direction) seems flatter than that for the higher proton energy (~3.7 MeV), which are consistent both in simulations and experiments, just as shown in Figs. 3(d), 3(e), and 3(n), and 3(o). The main reason is that the proton beam with lower energy always has worse directionality [40,41,51,52], resulting in a uniform distribution of the proton beam [see Figs. 3(d) and 3(n)]. In the contrast, the ring structure of the proton beam with higher energy is clearer [see Figs. 3(e) and 3(f)], which is consistent with the angular distribution in the Figs. 3(o) and 5(n). It should be noted that the initial ring structure of the proton beam in Fig. 5(l) will be maintained in the following progress, because plasma will be more neutral when the ions transport together with the electrons in the later time. Thus, it can be proven that a hollow proton beam can be driven by the hollow laser generated in our experiment, according to the comparisons in Fig. 5(l)–5(n). These hollow proton beams may have potential applications in concentrating the positron at the hollow center, calibrating the laser beam during multistage acceleration [41], in compact collimators for particles in rf accelerators [60], and so on.

In conclusion, the relativistic hollow laser is successfully generated by a reflected phase plate and then focused by a parabola in the experiments. Here, as the reflected phase plate functions like an ordinary mirror with a high reflective coating, it can be used in the present high-repetition petawatt (PW) laser systems. A simple optical model confirms that the relativistic hollow laser with $\mathrm{LG}_{p=0}^{l=1}$ mode may be generated by such a novel optical scheme.

Driven by the relativistic hollow laser, hollow plasma drill and acceleration have been experimentally achieved for the first time. With the development of intense laser technology, our research paves a path for the convenient production of high-repetition relativistic hollow lasers, which is important for a wide range of applications, such as the hollow particle acceleration proposed in this Letter, vortex manipulation on particles [16,17], vortex harmonics generation [29,30], huge magnetic field generation during vortex acceleration [32,33], and even jet research in the astrophysical environment [61].

This study was supported by the National Natural Science Foundation of China (Grant No. 11575274), Strategic Priority Research Program of the Chinese Academy of Sciences (Grant No. XDB16010600), Key Research Programs in Frontier Science (Grant No. ZDBS-LY-SLH006), and Shanghai special science and technology innovation supported project (Grant No. 2019-jmrh1-kj1). We would like to thank Dr. Junjie Yu and Dr. Yi Xu for the helpful discussion.

[*]Corresponding authors.
wangwenpeng@siom.ac.cn
[†]Corresponding authors.
ruxinli@siom.ac.cn
[‡]Corresponding authors.
zzxu@mail.shcnc.ac.cn
[§]These authors contributed equally to this work.

[1] L. Allen, M. W. Beijersbergen, R. J. C. Spreeuw, and J. P. Woerdman, Phys. Rev. A **45**, 8185 (1992).
[2] H. He, M. E. J. Friese, N. R. Heckenberg, and H. Rubinsztein-Dunlop, Phys. Rev. Lett. **75**, 826 (1995).
[3] M. E. J. Friese, J. Enger, H. Rubinsztein-Dunlop, and N. R. Heckenberg, Phys. Rev. A **54**, 1593 (1996).
[4] N. B. Simpson, K. Dholakia, L. Allen, and M. J. Padgett, Opt. Lett. **22**, 52 (1997).
[5] A. Ashkin, Phys. Rev. Lett. **24**, 156 (1970).
[6] A. Jesacher, S. Furhapter, S. Bernet, and M. Ritsch-Marte, Phys. Rev. Lett. **94**, 233902 (2005).
[7] B. Jack, J. Leach, J. Romero, S. Franke-Arnold, M. Ritsch-Marte, S. M. Barnett, and M. J. Padgett, Phys. Rev. Lett. **103**, 083602 (2009).
[8] M. F. Andersen, C. Ryu, P. Cladé, V. Natarajan, A. Vaziri, K. Helmerson, and W. D. Phillips, Phys. Rev. Lett. **97**, 170406 (2006).
[9] M. Padgett and R. Bowman, Nat. Photonics **5**, 343 (2011).
[10] J. Wang *et al.*, Nat. Photonics **6**, 488 (2012).
[11] N. Bozinovic, Y. Yue, Y. Ren, M. Tur, P. Kristensen, H. Huang, A. E. Willner, and S. Ramachandran, Science **340**, 1545 (2013).
[12] G. Molina-Terriza, J. P. Torres, and L. Torner, Nat. Phys. **3**, 305 (2007).
[13] F. Tamburini, B. Thidé, G. Molina-Terriza, and G. Anzolin, Nat. Phys. **7**, 195 (2011).
[14] G. A. Mourou, T. Tajima, and S. V. Bulanov, Rev. Mod. Phys. **78**, 309 (2006).
[15] D. Strickland and G. Mourou, Opt. Commun. **56**, 219 (1985).
[16] W. P. Wang, C. Jiang, B. F. Shen, F. Yuan, Z. M. Gan, H. Zhang, S. H. Zhai, and Z. Z. Xu, Phys. Rev. Lett. **122**, 024801 (2019).
[17] W. Wang, B. Shen, X. Zhang, L. Zhang, Y. Shi, and Z. Xu, Sci. Rep. **5**, 8274 (2015).
[18] J. Vieira and J. T. Mendonça, Phys. Rev. Lett. **112**, 215001 (2014).
[19] J. T. Mendonça and J. Vieira, Phys. Plasmas **21**, 033107 (2014).
[20] X. Zhang, B. Shen, L. Zhang, J. Xu, X. Wang, W. Wang, L. Yi, and Y. Shi, New J. Phys. **16**, 123051 (2014).
[21] J. Vieira, J. T. Mendonca, and F. Quere, Phys. Rev. Lett. **121**, 054801 (2018).
[22] L. X. Hu, T. P. Yu, Z. M. Sheng, J. Vieira, D. B. Zou, Y. Yin, P. McKenna, and F. Q. Shao, Sci. Rep. **8**, 7282 (2018).
[23] L. X. Hu, T. P. Yu, H. Z. Li, Y. Yin, P. McKenna, and F. Q. Shao, Opt. Lett. **43**, 2615 (2018).
[24] C. Baumann and A. Pukhov, Phys. Plasmas **25**, 083114 (2018).
[25] L. B. Ju, C. T. Zhou, K. Jiang, T. W. Huang, H. Zhang, T. X. Cai, J. M. Cao, B. Qiao, and S. C. Ruan, New J. Phys. **20**, 063004 (2018).
[26] L.-X. Hu, T.-P. Yu, Y. Lu, G.-B. Zhang, D.-B. Zou, H. Zhang, Z.-Y. Ge, Y. Yin, and F.-Q. Shao, Plasma Phys. Controlled Fusion **61**, 025009 (2019).
[27] X. Wang, B. Shen, X. Zhang, W. Wang, J. Xu, L. Yi, and Y. Shi, Phys. Plasmas **22**, 043106 (2015).
[28] C. Brabetz, S. Busold, T. Cowan, O. Deppert, D. Jahn, O. Kester, M. Roth, D. Schumacher, and V. Bagnoud, Phys. Plasmas **22**, 013105 (2015).
[29] X. Zhang, B. Shen, Y. Shi, X. Wang, L. Zhang, W. Wang, J. Xu, L. Yi, and Z. Xu, Phys. Rev. Lett. **114**, 173901 (2015).
[30] A. Denoeud, L. Chopineau, A. Leblanc, and F. Quéré, Phys. Rev. Lett. **118**, 033902 (2017).
[31] S. Ali, J. R. Davies, and J. T. Mendonca, Phys. Rev. Lett. **105**, 035001 (2010).
[32] D. Wu and J. W. Wang, Plasma Phys. Controlled Fusion **59**, 095010 (2017).
[33] Y. Shi, J. Vieira, R. M. G. M. Trines, R. Bingham, B. F. Shen, and R. J. Kingham, Phys. Rev. Lett. **121**, 145002 (2018).
[34] C. Liu *et al.*, Phys. Plasmas **23**, 093120 (2016).
[35] X.-L. Zhu, M. Chen, T.-P. Yu, S.-M. Weng, L.-X. Hu, P. McKenna, and Z.-M. Sheng, Appl. Phys. Lett. **112**, 174102 (2018).
[36] Y. Shi, B. Shen, L. Zhang, X. Zhang, W. Wang, and Z. Xu, Phys. Rev. Lett. **112**, 235001 (2014).
[37] J. Vieira, R. M. Trines, E. P. Alves, R. A. Fonseca, J. T. Mendonca, R. Bingham, P. Norreys, and L. O. Silva, Nat. Commun. **7**, 10371 (2016).
[38] A. Leblanc, A. Denoeud, L. Chopineau, G. Mennerat, P. Martin, and F. Quéré, Nat. Phys. **13**, 440 (2017).
[39] D. Y. Yu, D. B. Zou, M. Y. Yu, T. P. Yu, Y. Yin, F. Q. Shao, H. B. Zhuo, C. T. Zhou, and S. C. Ruan, New J. Phys. **21**, 083003 (2019).
[40] W. P. Wang *et al.*, Plasma Phys. Controlled Fusion **58**, 025010 (2016).
[41] W. P. Wang *et al.*, Phys. Plasmas **25**, 063116 (2018).

[42] W. P. Wang *et al.*, Phys. Plasmas **26**, 043102 (2019).
[43] B. Richards and E. Wolf, Proc. R. Soc. Ser. A **253**, 358 (1959).
[44] D. W. Forslund and C. R. Shonk, Phys. Rev. Lett. **25**, 1699 (1970).
[45] J. Denavit, Phys. Rev. Lett. **69**, 3052 (1992).
[46] H. Zhang *et al.*, Phys. Rev. Lett. **119**, 164801 (2017).
[47] Y. Murakami, Y. Kitagawa, Y. Sentoku, M. Mori, R. Kodama, K. A. Tanaka, K. Mima, and T. Yamanaka, Phys. Plasmas **8**, 4138 (2001).
[48] P. Antici *et al.*, Phys. Plasmas **14**, 030701 (2007).
[49] K. V. Safronov *et al.*, JETP Lett. **88**, 716 (2008).
[50] W. P. Wang *et al.*, Appl. Phys. Lett. **101**, 214103 (2012).
[51] W. P. Wang *et al.*, Appl. Phys. Lett. **102**, 224101 (2013).
[52] W. P. Wang *et al.*, AIP Adv. **5**, 107214 (2015).
[53] S. H. Zhai *et al.*, Appl. Phys. Lett. **114**, 013509 (2019).
[54] M. A. Clifford, J. Arlt, J. Courtial, and K. Dholakia, Opt. Commun. **156**, 300 (1998).
[55] A. Macchi, F. Cattani, T. V. Liseykina, and F. Cornolti, Phys. Rev. Lett. **94**, 165003 (2005).
[56] A. P. L. Robinson, P. Gibbon, M. Zepf, S. Kar, R. G. Evans, and C. Bellei, Plasma Phys. Controlled Fusion **51**, 024004 (2009).
[57] W. P. Wang, B. F. Shen, X. M. Zhang, L. L. Ji, M. Wen, J. C. Xu, Y. H. Yu, Y. L. Li, and Z. Z. Xu, Phys. Plasmas **18**, 013103 (2011).
[58] W. P. Wang, B. F. Shen, X. M. Zhang, L. L. Ji, Y. H. Yu, L. Q. Yi, X. F. Wang, and Z. Z. Xu, Phys. Rev. ST Accel. Beams **15**, 081302 (2012).
[59] S. C. Wilks, A. B. Langdon, T. E. Cowan, M. Roth, M. Singh, S. Hatchett, M. H. Key, D. Pennington, A. MacKinnon, and R. A. Snavely, Phys. Plasmas **8**, 542 (2001).
[60] G. Stancari, A. Valishev, G. Annala, G. Kuznetsov, V. Shiltsev, D. A. Still, and L. G. Vorobiev, Phys. Rev. Lett. **107**, 084802 (2011).
[61] D. Lynden-Bell, Mon. Not. R. Astron. Soc. **341**, 1360 (2003).